



Kinking facilitates grain nucleation and modifies crystallographic preferred orientations during high-stress ice deformation



Sheng Fan^{a,*}, David J. Prior^a, Travis F. Hager^b, Andrew J. Cross^{b,c}, David L. Goldsby^b, Marianne Negrini^a

^a Department of Geology, University of Otago, Dunedin, New Zealand

^b Department of Earth and Environmental Science, University of Pennsylvania, Philadelphia, PA, USA

^c Department of Geology and Geophysics, Woods Hole Oceanographic Institution, Woods Hole, MA, USA

ARTICLE INFO

Article history:

Received 9 March 2021

Received in revised form 27 June 2021

Accepted 27 July 2021

Available online xxxx

Editor: A. Webb

Dataset link:

<https://doi.org/10.17632/tstn4krkt8.1>

Keywords:

ice

kinking

nucleation

crystallographic preferred orientation (CPO)

electron backscatter diffraction (EBSD)

ABSTRACT

Kinking is an important strain-accommodating process during crystal plastic deformation under relatively large stresses and may influence the mechanical properties of the Earth's lithosphere and planetary cryosphere. To better understand the origins, mechanisms, and microstructural effects of kinking, we present detailed microstructural analyses of coarse-grained ($\sim 1300 \mu\text{m}$) ice samples deformed under uniaxial compression at -30°C . Deformed samples show elongated (aspect ratio ≥ 4) kink domains developing within or at the tips of remnant original grains ($\geq 300 \mu\text{m}$, aspect ratio < 4). Small, equiaxed subgrains also develop along the margins of remnant grains. Moreover, many remnant grains are surrounded by mantles of small, recrystallized grains ($< 300 \mu\text{m}$, aspect ratio < 4). Together, these observations indicate that grain nucleation is facilitated by both kinking and dynamic recrystallization. Low- ($< 10^\circ$) and high-angle (mostly $> 10^\circ$, many $> 20^\circ$) kink bands within remnant grains have misorientation axes that lie predominantly within the basal plane. The c -axes of most kink domains are oriented sub-perpendicular to the sample compression axis, indicating that kinking may produce or modify a crystallographic preferred orientation. Kink band densities are highest within remnant grains that have basal planes sub-parallel to the compression axis—these data are inconsistent with models suggesting that (if kinking is the only strain-accommodating process) there should be higher kink band densities within grains that have basal planes oblique to the compression axis. One way to rationalize this inconsistency between kink models and experimental observations is that kinking and dynamic recrystallization are both active during deformation, but their relative activities depend on the crystallographic orientations of individual grains. For grains with basal planes sub-parallel to the compression axis, strain-induced grain boundary migration (GBM) is inhibited, and large strain incompatibilities can be relaxed via kinking when other processes such as subgrain rotation (SGR) recrystallization are insufficient. For grains with basal planes oblique to the compression axis, strain-induced GBM might be efficient enough to relax the strain incompatibility via selective growth of these grains, and kinking is therefore less important. For grains with basal planes sub-perpendicular to the compression axis, kink bands are seldom observed—for these grains, the minimum shear stress required for kinking exceeds the applied compressive stress, such that kinks cannot nucleate.

© 2021 Elsevier B.V. All rights reserved.

1. Introduction

Plastic deformation, accommodated by the high-temperature creep of rocks and minerals (including ice), is necessary for many geodynamic phenomena on the Earth and other planetary bodies, including subduction, mountain building, mantle convection, and glacial flow. Microstructural studies and numerical models show that high-temperature plastic deformation is facilitated by dynamic recovery and recrystallization (Urai et al., 1986), which counteract work hardening and give rise to mechanical weakening by min-

* Corresponding author.

E-mail addresses: sheng.fan@otago.ac.nz (S. Fan), david.prior@otago.ac.nz (D.J. Prior), thager94@gmail.com (T.F. Hager), across@who.edu (A.J. Cross), dgoldsbys@sas.upenn.edu (D.L. Goldsby), marianne.negrini@otago.ac.nz (M. Negrini).

¹ Department of Geology, University of Otago, 360 Leith Street, Dunedin, New Zealand.

imizing the strain energy associated with crystal lattice defects, e.g., dislocations (Derby and Ashby, 1987, Humphreys et al., 2017, Weertman, 1983). Dislocations tend to arrange themselves into low-energy configurations via dynamic recovery. Recovery often produces low-angle intragranular boundaries, whose misorientation increases as dislocations with the same polarity are added (Humphreys et al., 2017). Recrystallization, on the other hand, involves the creation and/or migration of grain boundaries (Poirier and Guillopé, 1979), which often give rise to grain nucleation via two common processes: grain boundary bulging and subgrain rotation (SGR) (Urai et al., 1986). Bulge nucleation occurs when a grain boundary segment bulges (i.e., migrates) into a neighbouring grain, typically to sweep out a region of high strain energy (i.e., high defect density). The grain boundary bulge may then be severed by either continued grain boundary migration or by the formation of a subgrain wall across the bulge neck, which becomes increasingly misoriented until it develops into a grain boundary (Halfpenny et al., 2006). Rotation recrystallization, on the other hand, occurs solely via the progressive misorientation of subgrain walls, which eventually become high-angle boundaries (at a misorientation of $\sim 10^\circ$; Drury and Pennock, 2007) to form a new, distinct grain.

Both bulging and rotation recrystallization, then, involve the nucleation of new, low-strain, sub-equant recrystallized grains at the expense of original, high-strain remnant grains. However, rocks deformed at high stresses may become subdivided by two additional processes—twinning (Burkhard, 1993, Ferrill et al., 2004, Lacombe, 2010) and kinking (Nishikawa and Takeshita, 1999)—which produce elongate, blocky domains encompassed by straight boundaries. Although twinning and kinking produce similar domain morphologies, they are fundamentally different. Twinning occurs around a specific crystallographic relationship—i.e., misorientation axis-angle pair—between the parent grain and twin domains. Kinking, on the other hand, produces sharp lattice bending without a specific misorientation axis/angle. Nevertheless, some orientations are more prone to kinking than others.

Kinking is widely observed during the plastic deformation of various minerals, including mica, quartz, plagioclase, calcite, olivine, and pyrite, among others (see review by Vernon, 2018). Numerous experimental/modelling studies have been carried out to understand the mechanics of kinking in minerals, single-crystal/polycrystal ice, and metals (Bell et al., 1986, Gay and Weiss, 1974, Humphreys et al., 2017, Marano et al., 2021, Weiss, 2003). These studies reveal that kinking is more prevalent in materials with strong mechanical (elastic and viscous) anisotropy (Barsoum, 2020). For example, Gay and Weiss (1974) found that kinking is controlled by the magnitude of shear stress resolved on easy-slip planes (e.g., the basal plane for ice and quartz). In other words, grains in hard-slip orientations are more prone to kinking. Such a relationship was quantified further by Honea and Johnson (1976) and Nishikawa and Takeshita (1999), who modelled the high-stress deformation of elastic multilayers and quartz, respectively. Their models show that the critical (minimum) shear stress required for kink activation depends on the orientation between the crystallographic basal plane and the compression axis: the critical stress is the highest when the basal plane is perpendicular or parallel to compression, and it is lowest when the basal plane is inclined 45° from the compression axis. Using transmission electron microscopy, Bell et al. (1986) proposed that kinking in mica develops via continuous crystal lattice bending due to the progressive addition of dislocations to kink walls, similar to the process of SGR (Poirier and Nicolas, 1975, Urai et al., 1986).

As a mechanically anisotropic mineral (Duval et al., 1983), ice-1h is also prone to kinking. Under relatively fast strain rates and/or large differential stresses, ice-1h often develops straight kink boundaries with both low and high misorientation angles, and misorientation axes lying predominantly within the basal (0001)

plane (Piazolo et al., 2015, Seidemann et al., 2020). To date, most studies on kinking in ice have focused on the structure of kink boundaries and the dislocations that comprise them, based on misorientation and Burgers vector analyses (Piazolo et al., 2015, Seidemann et al., 2020). Seidemann et al. (2020) also correlated the activity of kinking (i.e., the number of kink boundaries per grain) with the magnitude of differential stress. These observations indicate that kinking should play a key role in accommodating plastic deformation under high stress conditions. Though high stress conditions are rarely found in terrestrial ice—indeed, kinks are seldom reported in polar ice samples (Jansen et al., 2016)—kinking may accommodate plastic deformation in Earth's rocky lithosphere, and in the icy lithospheres of other planetary bodies (e.g., Europa, Titan) where ice is subjected to larger stresses and lower temperatures (see review by Journaux et al., 2020). However, we still lack a complete understanding of how kinking contributes to grain nucleation and the development of anisotropy (i.e., crystallographic preferred orientation, CPO), especially in ice. This is largely because previous studies examined relatively fine-grained ice samples deformed to large strains ($>20\%$) (e.g., Seidemann et al., 2020). Even with state-of-the-art quantitative microscopy (e.g., cryogenic electron backscatter diffraction; Prior et al., 2015) it is difficult to resolve intragranular substructures at a resolution finer than $\sim 5 \mu\text{m}$ in ice. Furthermore, features arising from nucleation via kinking might be overprinted by subsequent plastic deformation and dynamic recrystallization at large strains.

In this contribution, we present microstructural analyses of coarse-grained ($\sim 1300 \mu\text{m}$) ice samples deformed under uniaxial compression to $\sim 10\%$ strain at -30°C . Samples were deformed under different strain rates to test the influence of stress on the development of kinking. Using coarse-grained ice samples increases our ability to characterize local, intragranular deformation features. Our objectives are to study: (1) the origins (e.g., crystallographic controls) on intragranular (kink) boundary formation; (2) kinking as a grain nucleation process; and (3) the role of kinking in modifying bulk CPOs. By answering these questions, we aim to better understand the cryo-tectonics of icy satellites, as well as the high-stress deformation of terrestrial analogues such as quartz.

2. Method

2.1. Sample fabrication

Polycrystalline ice samples were fabricated using a flood-freeze method (Cole, 1979). Ice seeds with a particle size between 1.6 and 2 mm were produced by sieving crushed ice cubes frozen from deionized ultra-pure water. After that, the ice seeds were “wet sieved” by pouring liquid nitrogen over the ice seeds while sieving. Wet sieving helps to remove fine grains that electrostatically clump together—coarse-grained ice samples produced by dry sieving contain a significant population of unwanted fine grains (e.g., Qi et al., 2017). Ice seeds were packed into cylindrical moulds with an inner diameter of 25.4 mm. The packed moulds were evacuated to a near-vacuum state and equilibrated in a water ice bath (0°C) for ~ 40 minutes before being flooded with degassed deionized ultra-pure water at 0°C . The flooded moulds were immediately transferred to a -30°C chest freezer and placed vertically into cylindrical holes in a polystyrene block, with the base of moulds touching a copper plate at the bottom of the freezer. This procedure ensures the freezing front migrates upwards, minimizing any trapping of bubbles within the samples. After 24 hours, the ice samples were gently pushed out from the moulds using an Arbor press. Ice samples were cut and polished on both ends to limit their lengths to 1.5–2.0 times the sample diameter (25.4 mm) and to ensure that both ends were flat and perpendicular to the sample cylindrical axis. Each sample was encapsulated in a thin-walled

Table 1
Summary of mechanical and microstructural data.

Sample No.	Uniaxial true strain rate at the end of experiment, ~10% strain (s^{-1})	Uniaxial stress at the end of experiment, ~10% strain (MPa)	Grain size metrics (μm): Lower quartile/ Median / Higher quartile	Within each grain population:		
				Total number of grains/ % grains contain low-angle (4° – 10°) boundaries/ % grains contain low-angle ($>10^{\circ}$) boundaries	*Small, low-aspect-ratio (recrystallized grains)	*Big, low-aspect-ratio (remnant grains)
Undeformed	N/A	N/A	768/ 1293 / 1781	All 173/ 82%/ 21%		
PIL275	1.2E-5	5.13	37/ 51 / 74	11107/ 37%/ 10%	321/ 100%/ 98%	1055/ 65%/ 26%
PIL270	3.0E-5	6.27	45/ 62 / 91	4047/ 44%/ 14%	239/ 100%/ 97%	704/ 70%/ 29%
PIL271	6.0E-5	7.03	37/ 48 / 64	9165/ 26%/ 7%	224/ 100%/ 98%	1022/ 68%/ 26%

* Small grains: grain size $<300 \mu m$; big grains: grain size $\geq 300 \mu m$. Low aspect ratio: aspect ratio <4 ; high-aspect ratio: aspect ratio ≥ 4 .

indium jacket tube (~ 0.38 mm wall thickness) with the bottom already welded to a stainless-steel end-cap. The top of indium jacket was then welded (melted) onto a steel semi-internal force gauge, with a zirconia spacer placed between the force gauge and sample to thermally insulate the sample during welding. During welding, the sample was kept submerged in a $-60^{\circ}C$ ethanol bath.

2.2. Experimental set up and process

Uniaxial compression experiments were conducted in a cryogenic, triaxial gas-medium apparatus (Heard et al., 1990) housed in the Ice Physics Laboratory, University of Pennsylvania. The ice samples were uniaxially deformed at $-30^{\circ}C$, and at a nitrogen gas pressure of ~ 40 MPa, under constant displacement rates yielding true axial strain rates of $\sim 1E-5$, $3E-5$, and $6E-5/s$ that result in compressive stresses >5 MPa (Table 1; Sect. S1 of supplement). Experiments were terminated once the true axial strain reached $\sim 10\%$. After deformation, samples were extracted from the apparatus within ~ 15 minutes. Immediately after extraction, we progressively cooled samples to ~ -30 , -100 and $-196^{\circ}C$ over a further period of ~ 15 minutes to minimize thermal cracking due to a drastic temperature drop. Samples were thereafter stored in a liquid nitrogen dewar.

2.3. Cryo-EBSD data

We collected cryogenic electron backscatter diffraction (cryo-EBSD) data from a polished surface on each ice sample (following procedures described by Prior et al., 2015). Cryo-EBSD provides full crystallographic orientations and microstructural details down to $\sim 5 \mu m$ spatial resolution. The EBSD data were indexed (as ice-1h) at a typical rate of $\sim 90\%$. Full technical details are provided in Appendix A. We note that during the time frame of sample extraction, transportation, and preparation for cryo-EBSD, normal grain growth should be negligible (see Sect. S2 of supplement) and significant modifications in grain boundary geometry and CPO are unlikely (Hidas et al., 2017, Wilson et al., 2014).

2.4. Processing of cryo-EBSD data

Ice grains were constructed from raw EBSD pixel maps using the MTEX toolbox (Bachmann et al., 2011) with a grain boundary misorientation angle threshold of 10° . Grain size was calculated

as the diameter of a circle with area equal to the measured area of each grain. We first removed grains with diameters $<20 \mu m$, as they are likely to result from mis-indexing. Poorly constrained grains (i.e., grains with $<50\%$ indexed pixel coverage) were also removed. Next, we applied the MTEX “fill” function, which interpolates non-indexed pixels using a nearest-neighbour method—each non-indexed pixel is replaced by a pixel with the same orientation as its nearest indexed pixel. The “fill” function populates 5–8% of the map area with interpolated pixels (Sect. S3 of supplement). After that, we reconstructed grains using the interpolated EBSD data. Grains at the edges of EBSD maps were removed. High-angle boundaries are located where the misorientation between neighbouring pixels is $>10^{\circ}$. Low-angle boundaries were also calculated using a misorientation angle of 4 – 10° between neighbouring pixels. In this study, boundaries with misorientation angles $<4^{\circ}$ were not included in any analyses, since very low-angle misorientations produce large uncertainties in misorientation axis orientations (Prior, 1999). We measured two parameters that are commonly used to examine grain shape—aspect ratio and shape preferred orientation (SPO). Aspect ratio is defined as the quotient between the long and short axis lengths of an ellipse (convex hull) fitted to each grain. SPO measures the distribution of angles between a given vector (the compression (y) axis in this study) and the long axis of each grain.

2.4.1. Montage artefacts

During EBSD data acquisition, large area maps were acquired by combining >120 individual scan tiles. We encountered two common types of montage-related artefacts: (1) duplicated data points along stitches, and (2) horizontal or vertical (x-y) shifts between adjacent tiles. Duplicated data points, usually limited to a strip of 1–2 pixels in width, are observed along the edges of adjacent tiles in montaged maps. We eliminated duplicated data points at stitches by simply removing these repeated pixels (green arrows in Figs. 2(a)–4(a)) using an automated algorithm. Tile shifts appear as an x-y offset along grain boundaries in PIL271 (pointed by white arrows in Fig. 4(b)). Tile shifts only occur within limited areas, and only affect a very small percentage of grains ($<2\%$; Sect. S4 of supplement); thus, they are unlikely to introduce significant errors into our microstructural analyses.

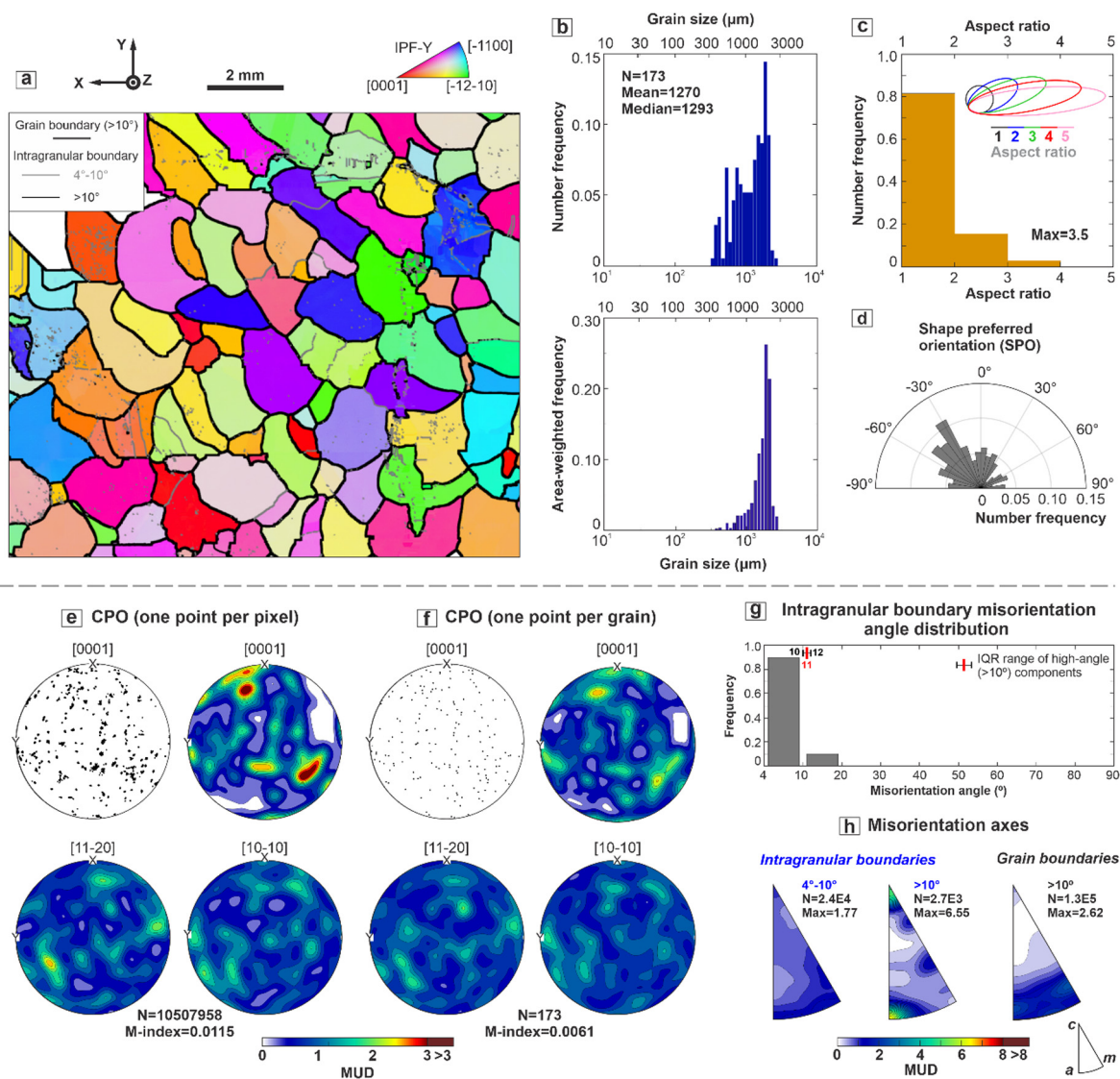


Fig. 1. Microstructural analyses of undeformed coarse-grained ice. The EBSD data collected with 5 μm step size are presented as (a) orientation map coloured by IPF-Y, which uses the colour map to indicate the crystallographic axes that are parallel to the y-axis as shown by the black arrows. Grain boundaries are black. Intragranular-boundaries are grey. We only show selected areas of EBSD maps so that the reader can resolve microstructural features. (b) Grain size statistics presented as grain size as a function of number frequency (**upper box**) or area-weighted frequency (**lower box**), with the grain size in logarithmic scale. (c) Distribution of aspect ratio. The max aspect ratio is marked within the box. Illustrative ellipses of different aspect ratios are also presented in the box. (d) Distribution of grain shape preferred orientation presented as a rose diagram for all grains. CPOs for [0001] (*c*-axes), [11-20] *a*-axes and [10-10] (pole to the *m*-plane) are plotted on the basis of (e) one point per pixel and (f) one point per grain. Contoured CPOs are coloured by multiples of a uniform distribution (MUD). (g) Distribution of misorientation angle for intragranular-boundaries. (h) Distribution of misorientation axes for intragranular-boundaries and grain boundaries (>10°) displayed as contoured inverse pole figures (IPFs) with crystal reference frame. (For interpretation of the colours in the figure(s), the reader is referred to the web version of this article.)

3. Results

3.1. Starting material

Undeformed coarse-grained ice samples exhibit a homogeneous microstructure with slightly irregular grain boundaries and a small number of intragranular (mostly low-angle) boundaries (Figs. 1(a, g)). Grain sizes follow a slightly right-skewed log-linear distribution, with a peak at $\sim 1300 \mu\text{m}$ and a tail extending down to $\sim 300 \mu\text{m}$ (Fig. 1(b)). Most grains are equant, with all grains having aspect ratios <4, and 80% of grains having aspect ratios <2 (Fig. 1(c)). Shape preferred orientation (SPO) is weak, with a slight bias towards grain long axes oriented $\sim 30^\circ$ from the sample compression axis (Fig. 1(d)). The starting material has a near-random CPO (Figs. 1(e-f)). Intragranular boundaries and grain boundaries have misorientation axes with near-random crystallographic ori-

entations, although there is a slight bias towards grain boundary misorientation axes lying within the basal plane (Fig. 1(h)).

3.2. Microstructure of deformed samples

3.2.1. Grain size statistics

All deformed samples contain large grains surrounded by networks of smaller grains (Figs. 2(a-b)–4(a-b)). All samples have similar arithmetic mean grain sizes, regardless of strain rate, much smaller than the average undeformed sample grain size (Table 1). Grain size histograms of deformed samples are bimodal, with peaks at 50–60 μm and 1000–2000 μm separated by a central minimum at $\sim 300 \mu\text{m}$ (Figs. 2(c)–4(c)). To interrogate the microstructures of these two grain size populations, we herein refer to grains smaller than 300 μm as *small* grains, and grains larger than or equal to 300 μm as *big* grains. To identify these specific terms, they will be written in italics herein. Area-weighted grain size his-

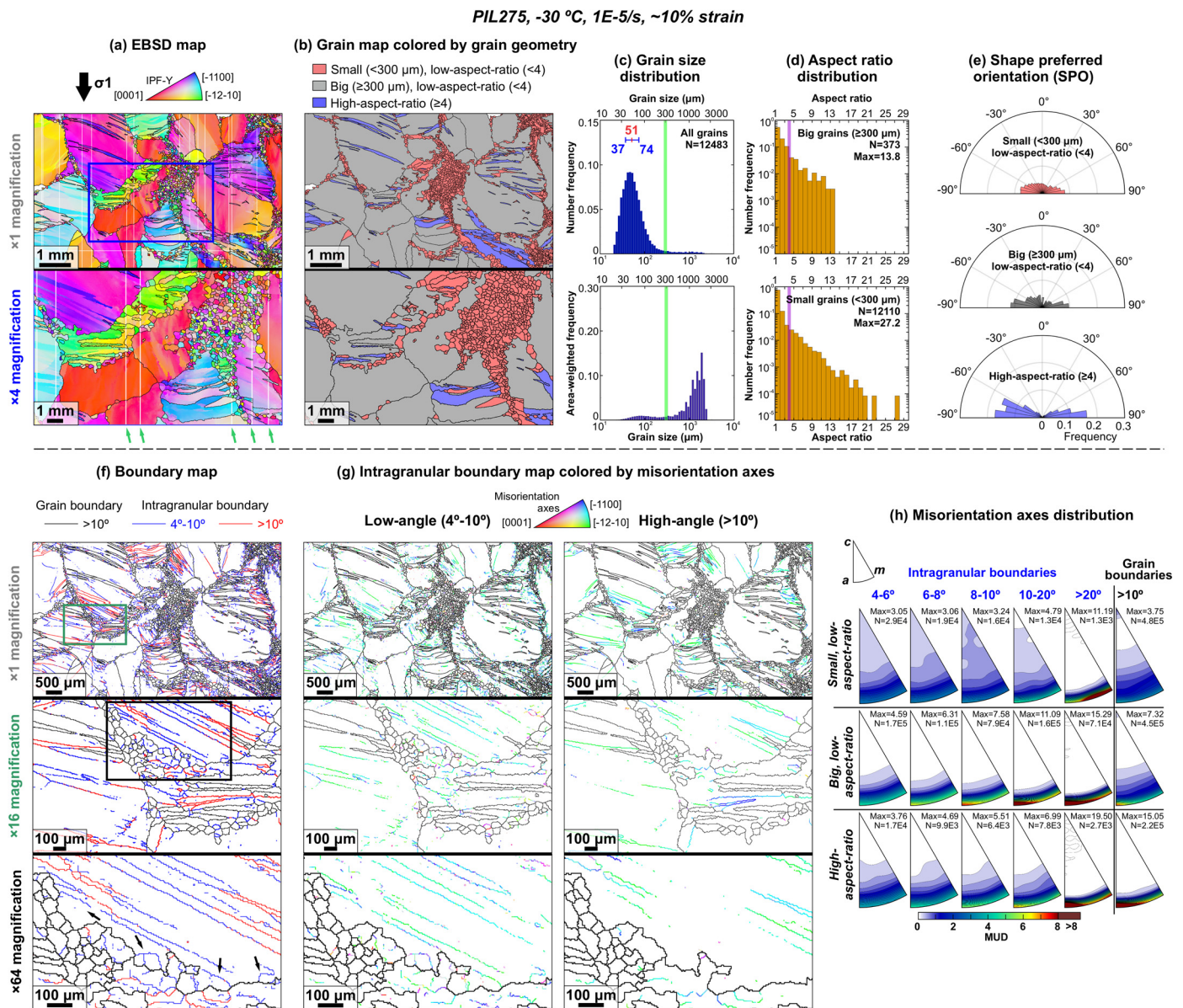


Fig. 2. Microstructural analyses of sample PIL275. **(a)** A sub-area of the orientation map. Orientation map is coloured by IPF-Y, which uses the colour map to indicate the crystallographic axes that are parallel to the vertical shortening direction as shown by the black arrow. Grain boundaries ($>10^\circ$) are shown black. **(b)** Grain map for grain populations with different sizes and shapes. **(c)** Grain size statistics presented as grain size as a function of number frequency (**upper box**) or area-weighted frequency (**lower box**), with the grain size in logarithmic scale. Interquartile range (IQR) of grain size is presented above the number-weighted grain size histogram. Median grain size is marked with red line, lower quartile and higher quartile grain sizes are marked with blue whiskers. **(d)** Distribution of aspect ratio for *big* (≥ 300 μm) and *small* (<300 μm) grains, with the y-axis (number frequency) in logarithmic scale. **(e)** Distribution of grain shape preferred orientation presented as rose diagrams for different grain populations. Colour scheme is the same as **(b)**. Radial dimension of bars corresponds to frequency with the scale shown on the horizontal axis. **(f)** Boundary map. Black arrows indicate the intragranular-boundary structures along grain boundaries. **(g)** Intragranular-boundary maps coloured on the basis of misorientation axes. Misorientation axes are coloured by IPF colour code in crystal reference frame. **(h)** Distribution of misorientation axes in contoured inverse pole figures (IPFs) with crystal reference frame for different grain populations.

tograms reveal that *big* grains occupy $>75\%$ of the mapped area in each deformed sample (Figs. 2(c)–4(c)). Note that the *small* grain population does not exist in the undeformed sample (Fig. 1(b)).

3.2.2. Grain populations

Deformed samples contain a significant number of “grains” (domains) with high aspect ratios (≥ 4) and relatively straight grain boundaries (Figs. 2(b, d)–4(b, d)), which are not observed in the undeformed material (Fig. 1(c)). These high aspect ratio, straight-sided domains develop within the interiors of *big* grains, particularly near the tips of those grains (Figs. 2(a, b)–4(a, b)). We identify these high aspect ratio grains as kink domains and separate them out for further analysis using an aspect ratio threshold of 4 (i.e.,

“grains” with aspect ratios ≥ 4 are treated as kink domains). The SPO of kink domains shows a strong maximum around $\sim 90^\circ$ from the compression axis (Figs. 2(e)–4(e)), indicating that kink domain long axes tend to lie in the plane normal to the compression direction. The SPO of grains with relatively low aspect ratios (<4), on the other hand, is weaker (Figs. 2(e)–4(e)). In deformed samples, grains with low aspect ratios have similar distributions of basal plane orientations as in the undeformed sample (compare the red histogram and black circles in Fig. 5(a)), which closely follow the expected distribution of basal plane orientations for a random CPO (green curve, Fig. 5(a)). Kink domains, on the other hand, tend to have a greater proportion of basal planes oriented at low angles (0 – 30°) to the compression direction (blue histogram, Fig. 5(a)).

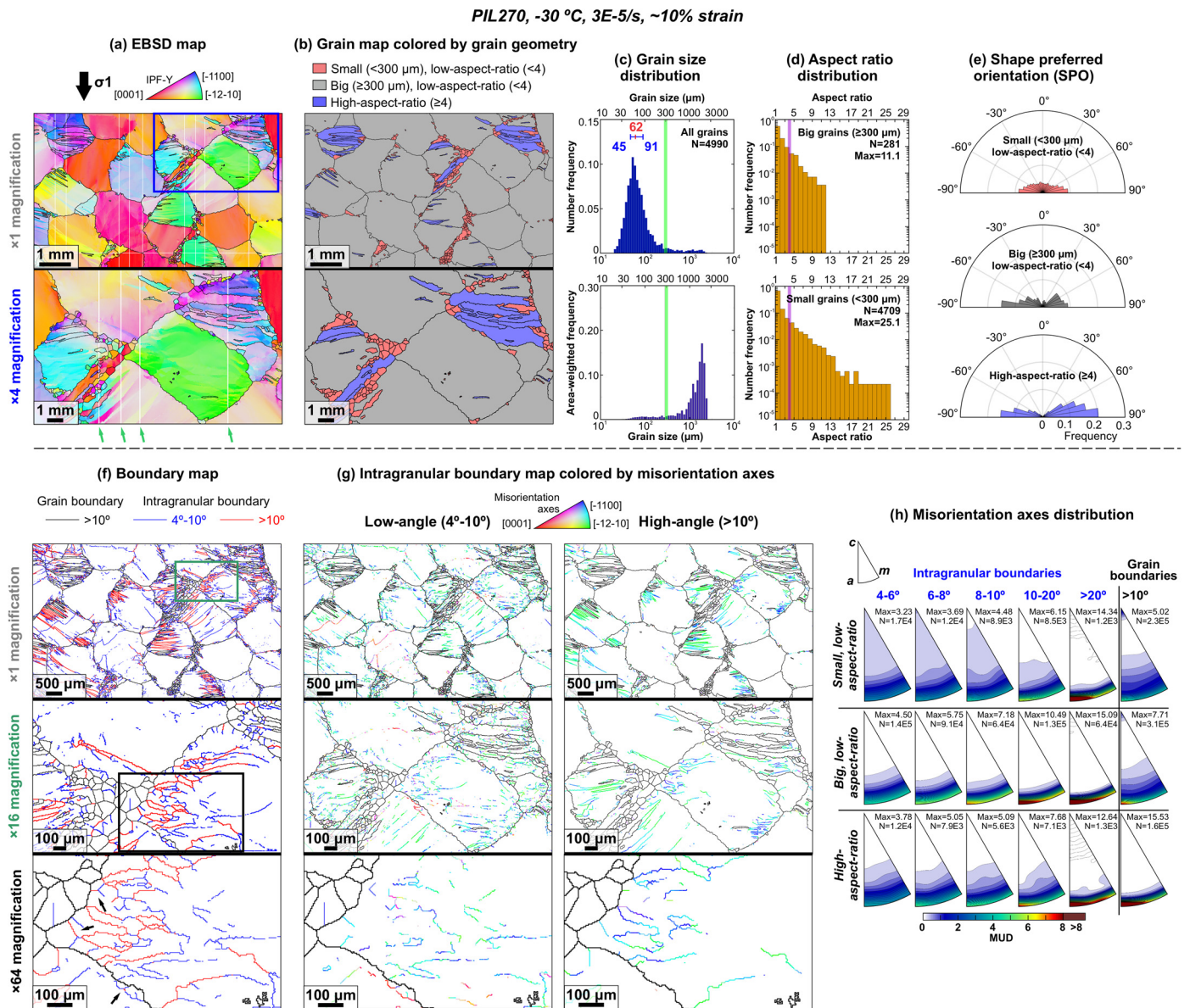


Fig. 3. Microstructural analyses of sample PIL270. The descriptions of (a) to (h) are the same as in Fig. 2.

In deformed samples, almost all the *big* grains with low aspect ratios (<4) contain intragranular boundaries—note that unless specified otherwise, “intragranular boundaries” herein refers to boundaries of all misorientation angles, both high (>10°) and low (4–10°). Note also that high-angle intragranular boundaries are non-closing, and therefore do not qualify as grain (i.e., intergranular) boundaries (which are defined as ≥10° boundaries that fully enclose a region). The frequency of *small* grains containing intragranular boundaries is low, particularly for *small* grains with low aspect ratios (<4) (Table 1). These observations suggest *small* low-aspect-ratio grains, which do not appear in the starting material (Fig. 1(c)), are less internally deformed and are likely to be nuclei produced by dynamic recrystallization. Accordingly, we herein refer to *small* grains with aspect ratios <4 as recrystallized grains. *Big* grains with low aspect ratios (<4) are widely observed in the starting material (Figs. 1(a, c)) and are therefore referred to as remnant grains. Recrystallized grains have a near-random grain boundary misorientation axes distribution, distinct from remnant grains and kink domains, which show primary maxima of boundary misorientation axes within the ice basal plane (Figs. 2(h)–4(h)).

For PIL275 and PIL271, the clustering of recrystallized grains can be observed at triple junctions of remnant grains (Figs. 2(b), 4(b)).

3.2.3. Intragranular boundary characteristics

For all deformed samples, intragranular boundaries comprise low-angle (<10°) and high-angle (>10°) components (Figs. 2(f)–4(f)). High-angle intragranular boundaries are mostly straight or slightly curved. Similarly, low-angle intragranular boundaries are mostly straight or slightly curved, although a small number have strong curvature (Figs. 2(f, g), 3(f, g), 4(f, g)). Furthermore, intragranular boundaries usually intersect the exterior boundary of their parent *big* grain on one side and terminate within their parent *big* grain at the other end; in other words, intragranular boundaries typically do not completely bisect their parent *big* grain (Figs. 2(f, g)–4(f, g)).

Many (low- and high-angle) intragranular boundaries—and particularly kink band boundaries—have misorientation axes lying within the basal plane, as indicated by a dominance of green-to-cyan-to-blue colours in boundary misorientation axis maps (Figs. 2(g)–4(g)). Misorientation axes are plotted in contoured inverse pole figures (Figs. 2(h)–4(h)). Intragranular boundary misori-

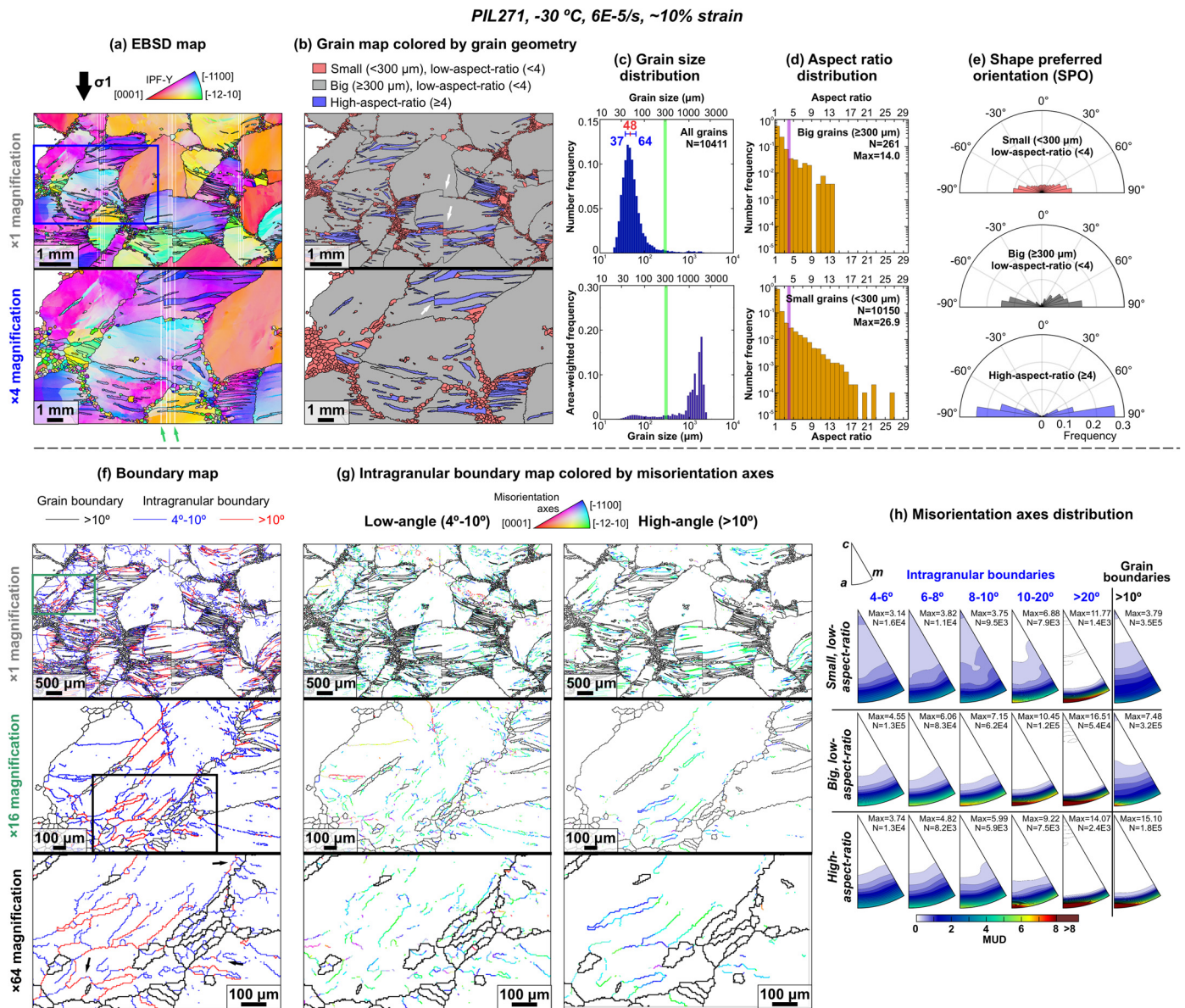


Fig. 4. Microstructural analyses of sample PIL271. The descriptions of (a) to (h) are the same as in Fig. 2. The white arrows in (b) indicate artefacts of shift between adjacent tiles within montaged EBSD data (Sect. 2.4.1).

entation axis distributions do not change substantially with strain rate. All grain populations show similar distributions of low- and high-angle intragranular boundary axes, characterized by primary maxima within the basal plane (Figs. 2(h)–4(h)). However, the intensity of maxima is greater for high-angle intragranular boundaries than for low-angle intragranular boundaries (Figs. 2(h)–4(h)).

3.2.4. Misorientation statistics and density of kink bands within remnant grains

We isolated intragranular boundaries that have misorientation axes lying within 1° of the ice basal plane (i.e., kink bands, Sect. 3.2.3) within remnant grains to further quantify their misorientation statistics. For all deformed samples, the misorientation angle distribution of kink band boundaries exhibits a unimodal distribution with a peak at the cut-off misorientation angle of 4° and a tail extending to misorientation angles up to 60–70° (grey bars in Fig. 5(b)). Most (>60%) kink band boundaries have misorientation angles larger than 10°, and a considerable proportion (>20%) have misorientation angles >20° (red lines in Fig. 5(b)). In contrast, the few kink band boundaries found within the undeformed start-

ing material have misorientation angles mostly <10° (pink lines in Fig. 5(b)).

For each remnant grain, we calculated the density of kink bands—i.e., the total length of kink bands per grain area—as a function of the angle between the mean grain basal plane orientation and the compression axis (Fig. 5(c)). The frequency of *c*-axes observed from a 2-D surface generally increases as the angle between *c*-axis and compression axis increases (Fig. 5(a)). However, such stereological issue should have little impact on the statistics of kink band densities (Sect. S5 of supplement). Remnant grains generally have significantly higher kink band densities after deformation (Fig. 5(c)). Furthermore, within deformed samples (and regardless of strain rate), kink band density gradually decreases as grain basal planes become more steeply inclined with respect to the compression axis, such that grains with basal planes normal to the compression axis have the lowest kink band densities.

3.3. Crystallographic preferred orientation (CPO)

For each sample, we calculated the CPO of all grains, remnant grains, recrystallized grains, and kink domains (Fig. 6(a)), using

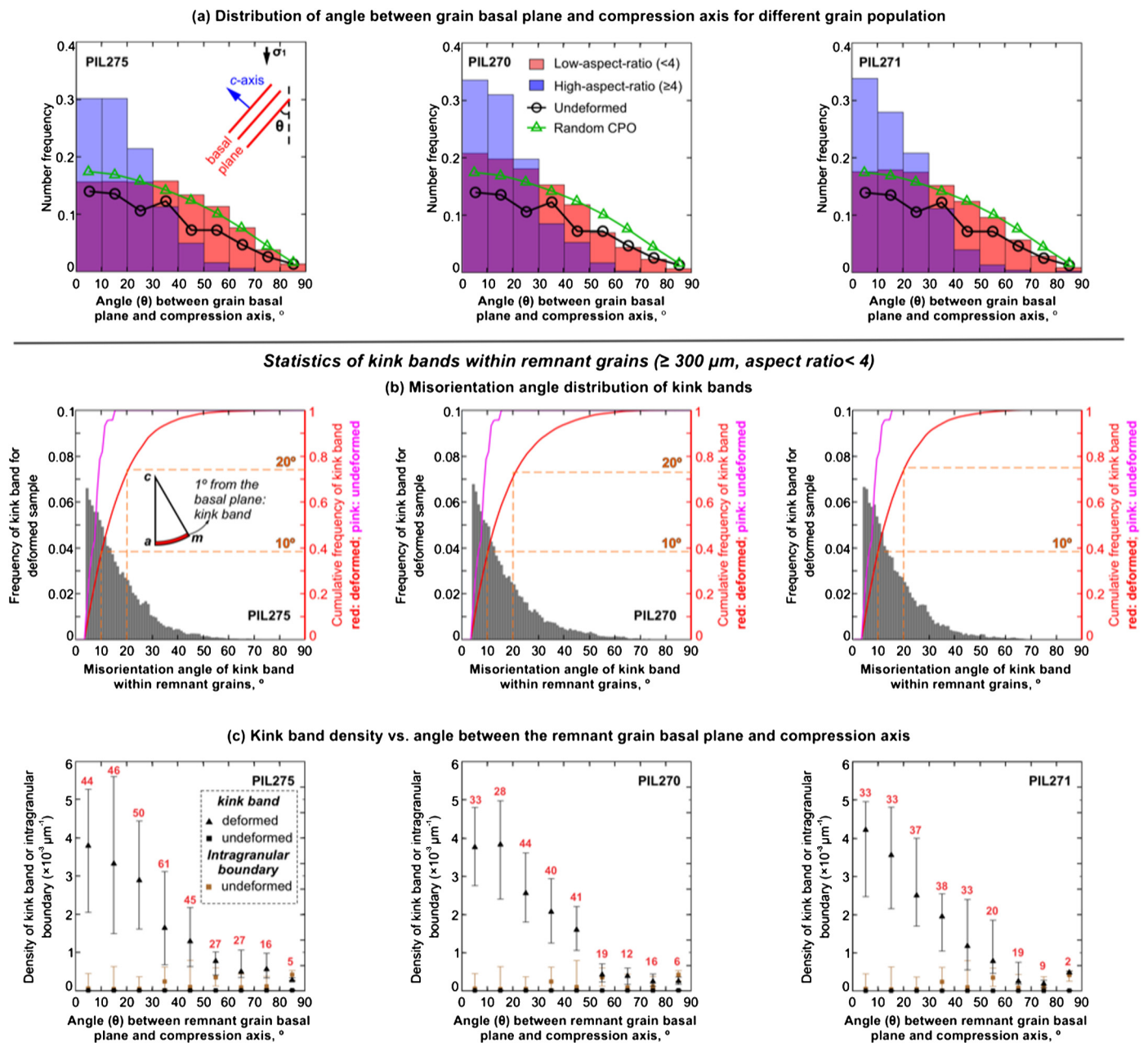


Fig. 5. (a) Number frequencies of high- and low-aspect-ratio grains with basal planes at 10° intervals to the compression axis. (b) Bar plots (grey, corresponds to the left y-axis) represent misorientation angle distribution of kink-band, i.e., intragranular-boundary with misorientation axis within 1° to the ice basal plane, for deformed sample. Line plots (corresponds to the right y-axis) represent cumulative frequency of kink-band as a function of misorientation angle for deformed sample (red) and undeformed sample (pink). (c) Distribution of kink-band density as a function of the angle between basal plane and compression axis for remnant grains ($\geq 300 \mu\text{m}$, aspect ratio < 4) for deformed sample (black triangle). These data are compared with the kink-band density (black square), i.e., the length of kink-band per grain area, as well as intragranular-boundary density (brown square), i.e., the length of intragranular-boundary per grain area, of all grains within undeformed sample. Kink-band and intragranular-boundaries comprise low- (4° - 10°) and high-angle ($>10^\circ$) components. Distribution of kink-band or intragranular-boundary density is visualized as whiskers indicating lower quartile and higher quartile and a triangle or square indicating median value. At each angle interval, the number of remnant grains in deformed samples used for calculation is marked in red.

both the orientations of all pixels and the mean orientation of each grain. Here we discuss the CPOs calculated from all pixels, for simplicity, although the mean-orientation CPOs are very similar (Sect. S6 of supplement). CPO intensity is calculated using the M-index (Skemer et al., 2005). The *c*-axis CPOs (pole figures) are summarized in Fig. 6(b).

3.3.1. All grains and remnant grains

Pole figures for all grains and remnant grains are very similar, both characterized by three to four *c*-axes maxima lying within a poorly defined open cone (small circle) or possibly cluster centred

at $\sim 45^\circ$ to the compression axis (Fig. 6). The *c*-axes open cone is subtly more blurred for PIL275 ($\sim 1\text{E-}5/\text{s}$) and PIL270 ($\sim 3\text{E-}5/\text{s}$) than for PIL271 ($\sim 6\text{E-}5/\text{s}$). The *a*-axes and poles to the *m*-plane lie within a broad, poorly defined girdle normal to the compression axis.

3.3.2. Kink domains

Kink domains exhibit the strongest CPO of the different grain populations, as indicated by the relatively high M-index values (Fig. 6(a)). The *c*-axes of kink domains generally lie near the plane normal to the compression axis (Figs. 6(a, b)). The *a*-axes and

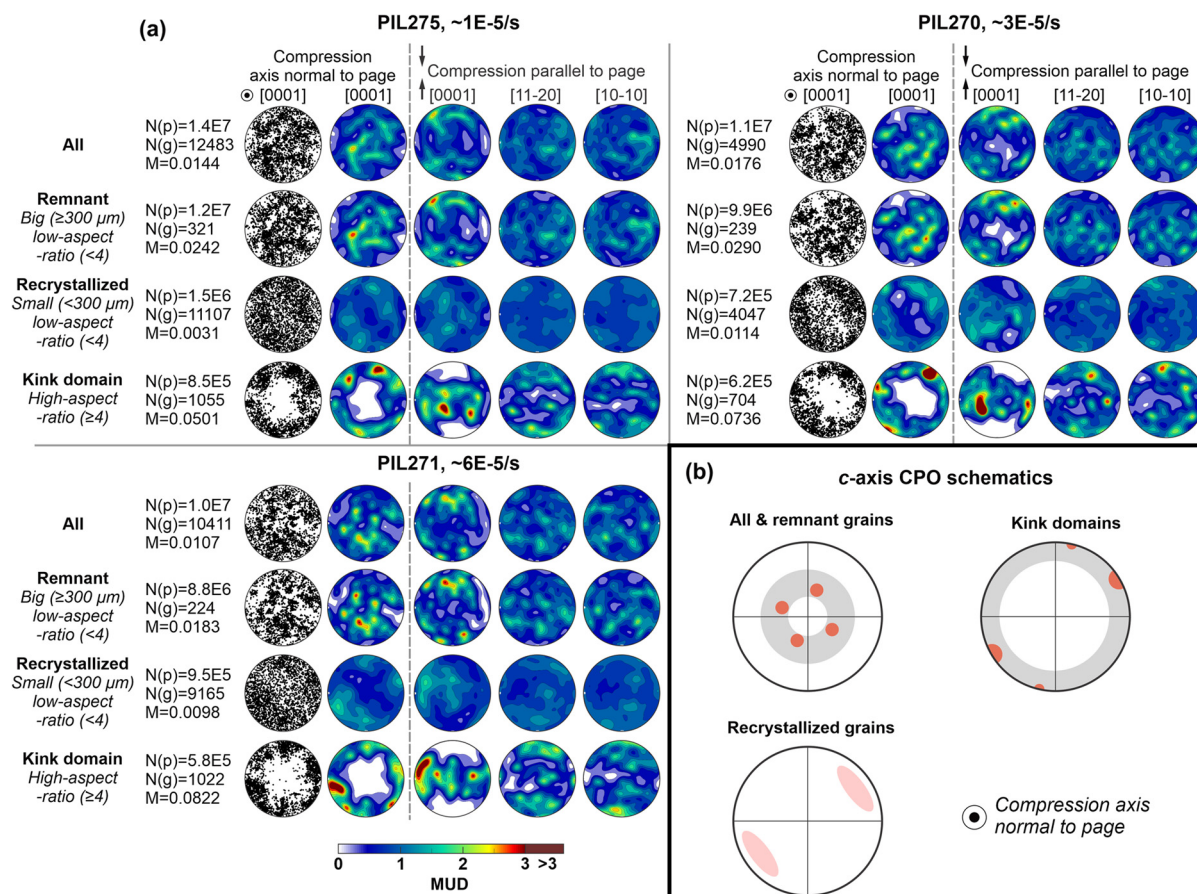


Fig. 6. (a) Crystallographic preferred orientation (CPO) analyses using orientation data of all pixels for all grains and different grain populations. CPOs of different samples are presented in separate boxes. Within each box, the grain population name, grain number (N(g)), the number of pixels used for calculation (N(p)) and M-indices (M) are presented in the first column. The distributions of [0001] (*c*-axes) orientations plotted as point pole figures with 5000 randomly selected points and contoured pole figures are presented in the second and third column, respectively, with the compression axis perpendicular to page. The distributions of orientations for [0001] (*c*-axes), [11 $\bar{2}$ 0] *a*-axes and [10 $\bar{1}$ 0] (poles to the *m*-plane), with the compression axis vertical, are presented in the fourth, fifth and sixth column, respectively. (b) Summary of *c*-axis CPO schematics for different grain populations from (a).

poles to the *m*-plane define a weak narrow cone or cluster centred around the compression axis (Fig. 6(a)).

3.3.3. Recrystallized grains

Recrystallized grains have the weakest CPOs of the different grain populations (see M-index values; Fig. 6(a)). Their *c*-axes define a weak broad maximum, lying within the plane containing the compression axis, but centred around an axis inclined $\sim 45^\circ$ from the compression axis. Although the deformation (uniaxial compression) geometry has axial symmetry around the compression axis, the *c*-axis pole figures are not axially symmetric (Fig. 6(b)). The *a*-axes and poles to the *m*-plane have a near-random distribution.

4. Discussion

4.1. Microstructural development

The undeformed coarse-grained ice exhibits a more irregular grain boundary geometry than fine-grained ($\sim 300 \mu\text{m}$) ice samples fabricated via the same “flood-freeze” method (Fan et al., 2021, 2020). Moreover, although the “wet sieve” method (Sect. 2.1) is more effective than the “dry sieve” method (cf., Qi et al., 2017) for removing unwanted finer grains, our starting material contained a non-negligible number fraction of grains with diameters $< 1000 \mu\text{m}$, which comprise $< 10\%$ area fraction (Fig. 1(b)). Annealing the sample prior to deformation might help to further improve

the fabrication of coarse-grained ice to achieve a more homogeneous starting microstructure.

4.1.1. Nucleation

Subgrain rotation (SGR) recrystallization In all deformed samples, “core-and-mantle” structures (White, 1976)—i.e., networks of small, recrystallized grains encircling remnant, big grains—are well developed (Figs. 2(b)–4(b)). Moreover, equiaxed subgrains (defined by curved intragranular boundaries intersecting grain boundaries of the host remnant grains) are widely observed within deformed samples (black arrows in Figs. 2(f)–4(f)). Core-and-mantle structures and subgrains along the margins of remnant grains are typical of SGR recrystallization (Halfpenny et al., 2006; Poirier and Nicolas, 1975; Urai et al., 1986). Bulging nucleation and spontaneous nucleation may also contribute to recrystallized grain formation, but their relative contributions are difficult to determine without *in situ* observation (e.g., Herwegh et al., 1997).

The number of grains per unit area (accounting for multiple occurrences of the same 3-D grain) is much higher in deformed samples than undeformed samples (details in Sect. S7 of supplement; method in Fan et al., 2021, 2020), suggesting nucleation is involved in the recrystallization. We also observe localized clusters of recrystallized grains near triple junctions between remnant grains (Figs. 2(b), 4(b); Sect. 3.2.2). These clusters may arise from focused nucleation controlled by local grain orientations and strain incompatibilities. For instance, “soft” grains in easy-slip orientations can accommodate more strain, which may enhance the dynamic recov-

ery, and therefore favour dynamic recrystallization in these grains (Schmid, 1994; Wenk et al., 1991). Moreover, strain incompatibilities at three-grain junctions can be resolved by locally increasing the dislocation density, which then drives recrystallization in these regions (Chauve et al., 2017a).

Grain segmentation via kinking Kink domains encompassed by high-angle boundaries are widely developed within all deformed samples (Sect. 3.2.2). Thus, in addition to grain nucleation by SGR recrystallization, new grain boundary area is also formed via kinking, which leads to further grain segmentation and grain size reduction. In other words, kinking also acts as a grain nucleation mechanism, forming new high-aspect-ratio grains (kink domains) at the expense of remnant grains. The low strain samples examined here do not show extensive segmentation within kink domains (Figs. 2–4); however, at high strains, further segmentation of kink domains might result from progressive nucleation (Seidemann et al., 2020).

4.1.2. Kink band characteristics

Straight or slightly curved intragranular boundaries are widely observed (Figs. 2(f)–4(f)), with low- and high-angle misorientation axes lying predominantly within the basal plane (Figs. 2(g, i)–4(g, i)), matching kink band observations from previous ice studies (Piazolo et al., 2015; Seidemann et al., 2020). Most (~60%) kink band boundaries have misorientation angles $>5\text{--}10^\circ$, and a considerable proportion ($>20\%$) have misorientation angles $>20^\circ$ (Fig. 5(b)). Therefore, although kink bands can become highly misoriented with respect to their parent grain, kink bands remain strongly crystallographically controlled, with misorientation axes lying within the basal plane.

Misorientation statistics of kink bands can help us to better understand SGR, since kinking and SGR follow very similar kinematics—they both involve a continuous crystal lattice bending due to the progressive addition of dislocations to kink or subgrain walls (Bell et al., 1986; Poirier and Nicolas, 1975; Urai et al., 1986). Indeed, in our samples the frequency of kink band boundaries decreases continuously from low (4°) to high ($60\text{--}70^\circ$) misorientation angles (Fig. 5(b)), suggesting that kinking results from continuous lattice bending, rather than an instantaneous lattice bending that would immediately form a large proportion of high-angle boundaries. Based on these observations, we suggest that the subgrain walls can become similarly misoriented to high angles ($>20^\circ$) while maintaining a near-constant misorientation axis. Thus, observations of near-random grain boundary misorientation axis distributions within recrystallized networks (and between recrystallized and remnant grains) (Figs. 2(h)–4(h)) may warrant re-examination. It is commonly assumed that low-angle dislocation arrays (i.e., subgrain walls) and their misorientation relationships break down above a certain misorientation angle, as the boundary cannot maintain a dislocation structure to higher angles (Humphreys et al., 2017). Perhaps, instead, other processes cause boundary misorientation axes to change. For example, the coalescence of intragranular boundaries to form high-angle grain boundaries can allow other processes—such as grain boundary sliding and grain boundary migration—to proceed, which may then modify grain boundary structures and misorientation axes (Ree, 1994).

4.2. Crystallographic controls and effects of kinking

At low ($\sim 1\text{E-}5\text{/s}$) and median strain rates ($\sim 3\text{E-}5\text{/s}$), remnant grains have *c*-axes loosely smeared in an open cone (small circle) near easy slip orientations (Figs. 6(a–b))—i.e., *c*-axes at $\sim 45^\circ$ to compression. Cone and cluster CPOs are commonly observed in ice samples deformed under uniaxial compression conditions, and

are thought to arise from varying contributions of strain-induced grain boundary migration (GBM) and grain rotation due to dislocation glide (Kamb, 1972). At high strain rates ($\sim 6\text{E-}5\text{/s}$), on the other hand, smearing of *c*-axes is not obvious; instead, *c*-axes form multiple-maxima point clusters (Fig. 6(a)). Smearing of *c*-axes at lower strain rates indicates progressive intragranular distortions of remnant grains within easy slip orientations. At higher strain rates, *c*-axes may be less smeared as kinking and dynamic recrystallization become more efficient, and therefore accommodate part of the strain that is otherwise accommodated via intragranular distortions at lower strain rates (e.g., Herwegh et al., 1997). However, multiple-maxima ice *c*-axis fabrics such as those observed at high strain rates may also arise when the number of grains measured from a single sample plane is not sufficient for a fully representative CPO (Monz et al., 2021).

Recrystallized grains have a CPO that is much weaker than the other grain populations (Sect. 3.3.3). Weak recrystallized grain CPOs have been reported in previous studies on experimentally deformed ice (Fan et al., 2020) as well as naturally and experimentally deformed rock (Bestmann and Prior, 2003). Various processes have previously been invoked to explain CPO weakening of recrystallized grains, including grain boundary sliding (Warren and Hirth, 2006), bulging nucleation (Falus et al., 2011) and spontaneous nucleation (Herwegh et al., 1997).

Kink domains exhibit a *c*-axis girdle within the plane normal to the compression axis, forming a CPO that is distinct from remnant and recrystallized grains (Fig. 6). Nevertheless, at $\sim 10\%$ strain in this study, the CPO of all grains (bulk CPO) is similar to the CPO of remnant grains alone, suggesting kink domains have a weak influence on the bulk CPO at low strains. Further studies should be conducted to investigate the influence of kink domains in the modification of bulk CPO at high strains.

4.2.1. Grain orientation controls on kinking activity

Previous studies suggest that materials with strong mechanical anisotropy, like ice-1h, are prone to kinking (Piazolo et al., 2015; Seidemann et al., 2020). Furthermore, deformation experiments on mechanically anisotropic metals and geological materials (e.g., graphite, mica) show that kinks predominately form when basal planes are oriented poorly for easy-slip (see review by Barsoum, 2020). Thus, we might expect to see high kink band densities in host grains with basal planes oriented sub-parallel and sub-perpendicular to the compression axis (i.e., in grains with hard, low-basal-Schmid-factor orientations). However, while we find that kink band density is highest within remnant grains with basal planes oriented sub-parallel to the compression axis, there is almost a complete absence of kink bands within host grains that have basal planes oriented sub-perpendicular to the compression axis (Sect. 3.2.4; Fig. 5(a)). In other words, the activity of kinking does not simply correlate with basal Schmid factor, as suggested by previous kinking studies and models.

4.2.2. Modelling crystallographic controls on kink nucleation

Honea and Johnson (1976) introduced a 2-D numerical model to describe kinking within elastic multilayers with frictional contacts; they suggest that kink nucleation depends on the magnitude of both the applied stress and the effective friction between layers. More recent studies propose that the mechanism for kinking may be buckling within atomic planes of an elastic multilayer when loaded in compression (see review by Barsoum, 2020). To understand kinking within deformed quartz, Nishikawa and Takeshita (1999) further improved the model from Honea and Johnson (1976) by incorporating the angle (θ) between applied stress and the kink plane—i.e., the basal plane in the case of quartz and ice; they propose that under uniaxial compression, the critical

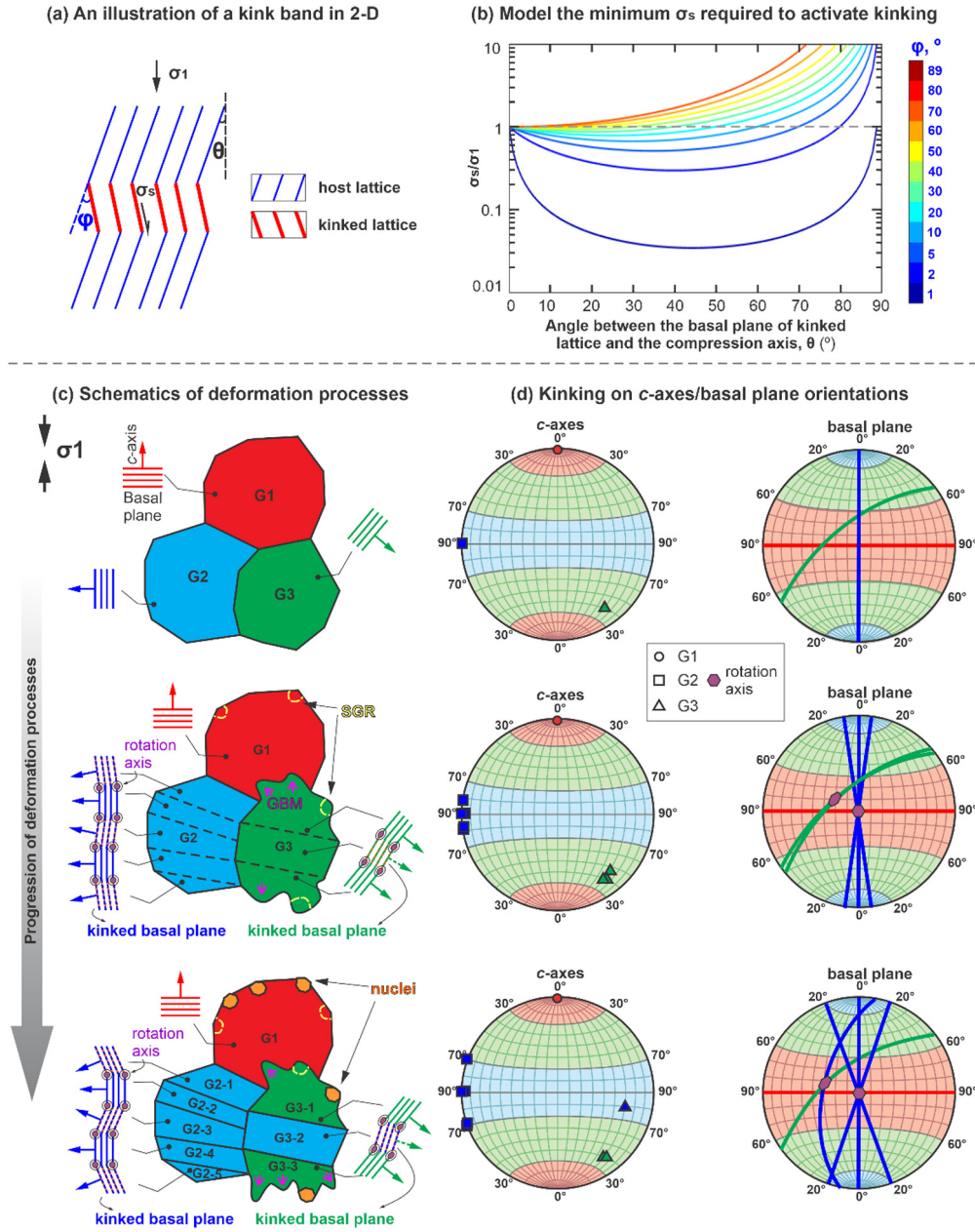


Fig. 7. (a) Schematic drawing illustrating a kink-band structure in 2-D. (b) Modelling results showing the minimum shear stress required for a kink-band to continue with the deformation should be a function of the angle between the basal plane of host lattice and compression axis as well as the rotation angle of the kink-band relative to the host lattice (Honea and Johnson, 1976, Nishikawa and Takeshita, 1999). (c) Schematic drawing of processes involved in the deformation of coarse-grained ice under uniaxial compression. GBM represents grain boundary migration; SGR represents subgrain rotation. For kinked lattices in (c), we draw the corresponding orientations of c-axes and basal planes in pole figures in (d).

shear stress, σ_s , required for a kink band to accommodate deformation in 2-D is as follows:

$$\sigma_s = \frac{\sigma_1}{\cos^2\theta + \frac{\sin\theta\cos\theta}{\tan\varphi}}, \quad (1)$$

where σ_1 is the maximum principal stress (i.e., stress along the compression axis in this case), φ is the misorientation angle between the basal plane of the kink band and the basal plane of its host lattice, and θ is the angle between the basal plane of the host lattice and the compression axis (Fig. 7(a)). Equation (1) implies that, for a host lattice (e.g., blue lines in Fig. 7(a)) containing one or more kink bands (e.g., red lines in Fig. 7(a)), the critical shear stress, σ_s , required for the kink bands to continue deforming depends on (1) the relative magnitudes of the stresses resolved on

the basal planes of kink bands and the basal planes of the host lattice, and (2) the relative orientation between the compression axis and the basal plane of the host lattice.

The model makes two predictions for polycrystalline aggregates deforming solely via kinking. First, that the critical shear stress required for a kink band to accommodate deformation, σ_s , increases as a kink band becomes more misoriented (increasing φ) with respect to its host grain; that is, it becomes harder for kink bands to develop as they become more misoriented with respect to their host grain. Second, the model predicts that for small kink-host misorientation angles (i.e., low φ —cool coloured curves in Fig. 7(b)), kink band density should be greatest in host grains with basal planes oblique ($\theta = 30^\circ$ – 50°) to the compression axis, because σ_s will be the lowest at these orientations. For large kink-host misorientation angles (i.e., high φ —hot coloured curves in Fig. 7(b)),

kink band density should be generally low, because σ_s is equal to or higher than the principal stress, σ_1 . Our experimental observations do not match the second model prediction. For kink boundary misorientation angles, φ , smaller than 20° —which are common in our samples (Fig. 5(b))—kink band densities should be greatest within remnant grains that have basal planes oblique to the compression axis ($\theta = 30\text{--}50^\circ$; Fig. 7(b)). In contrast, we find that remnant grains with basal planes parallel to the compression axis have the highest densities of intragranular boundaries, while remnant grains with basal planes normal to the compression axis have the lowest densities of intragranular boundaries (Fig. 5(b), Sect. 3.2.4). One way to rationalize the mismatch between the experimental observations and model predictions is that the 2-D model addresses deformation via kinking alone, and does not consider the complicated competition/balance amongst dynamic recovery, kinking and recrystallization processes in 3-D. Additionally, intergranular shearing—which might occur along straight kink band boundaries (Herwegh et al., 2005)—is not considered in the 2-D model, but may provide another driving force for kinking. We propose that the relative activity of these various processes will vary depending on the crystallographic orientation of each grain, providing additional controls on kink nucleation.

Fig. 7(c) schematically illustrates the relationship between ice c -axis/basal plane orientations and the activities of kinking, dynamic recovery, and recrystallization processes. Grains with basal planes oblique to the compression axis ($\theta = 30\text{--}50^\circ$; e.g., G3 (green), Fig. 7(c)) are optimally oriented for both kinking and easy-slip, i.e., dislocation glide on the ice basal plane. Previous studies suggest that strain incompatibilities can be efficiently relaxed through the selective growth of grains in easy-slip orientations via strain-induced grain boundary migration (GBM) (Fig. 7(d); e.g., Derby and Ashby, 1987, Humphreys et al., 2017, Schmid, 1994, Wenk et al., 1991). Therefore, kinking may be less important within grains in easy-slip orientations (i.e., with basal planes oblique to the compression axis here). Grain with basal planes sub-parallel to shortening ($\theta \approx 0^\circ$; e.g., G2 (blue), Fig. 7(c)), on the other hand, are unfavourably oriented for basal dislocation glide; thus, strain-induced GBM is inhibited, and strain incompatibilities must be accommodated predominately by kinking (Fig. 7(d)). For grains with basal planes sub-perpendicular to shortening ($\theta \approx 90^\circ$; e.g., G1 (red), Fig. 7(c)), the critical shear stress, σ_s , required for the progression of kinking exceeds the maximum principal stress, σ_1 , except perhaps at very small kink-host misorientation angles, $\varphi < 10^\circ$ (Fig. 7(b)). Thus, grains with basal planes sub-perpendicular to the compression axis are fundamentally stable and difficult to kink (Fig. 7(d)), consistent with our microstructural data showing that grains in these orientations have the lowest density of kink bands (Fig. 5(b)). At these orientations, where kinking is likely inhibited, dynamic recovery and recrystallization might play a primary role in relaxing strain incompatibilities via the production of subgrains and recrystallized grains at the cost of remnant grains and/or kink domains (Burkhard, 1993, Herwegh et al., 2005). Grains with basal planes oriented normal to the compression axis are stronger than grains with basal planes oriented parallel to the compression axis—the latter kink while the former do not—even though they are equally poorly oriented for basal dislocation glide. Strain in the hardest ($\theta \approx 90^\circ$) grains might therefore be accommodated by non-basal dislocation glide (e.g., Chauve et al., 2017b).

4.3. Implications for natural ice and rock deformation

In terrestrial glacial settings, kink bands have only been observed within folded ice layers, where local stresses and strain rates are relatively high (Jansen et al., 2016). Thus, kinking might have only a limited impact on the mechanics of terrestrial ice flow. However, for other planetary bodies (particularly those with icy

lithospheres) where ice is subject to large stresses and low temperatures (see review by Journaux et al., 2020), kinking might be important in controlling ice deformation. Our experimental data imply that under large stresses, kinking plays a key role in segmenting new grains from original grains (nucleation) (Sect. 4.1.1) and accommodating large plastic strain when thermally activated creep processes (e.g., vacancy diffusion and dislocation climb) are inefficient (Sect. 4.2), as may be the case in the cold outer solar system.

Ice is also an important analogue for the deformation of minerals such as quartz, for which deformation under temperatures close to the melting point is hard to achieve experimentally (e.g., Wilson et al., 2014). In this study, ice samples were deformed at a relatively high homologous temperature ($T/T_m \approx 0.9$) and fast imposed strain rates (producing relatively large differential stresses): conditions that may be relevant to localized lithospheric shear zones. Our new data suggest that kinking—and perhaps also twinning, which occurs frequently in minerals deformed under low temperature, high stress conditions (Herwegh et al., 1997, Honea and Johnson, 1976, Nishikawa and Takeshita, 1999)—should be important during high stress mineral deformation, at least at low strains. Future studies should focus on the evolution of kink bands at high strains—more specifically, the modification of kinking structures via strain-induced GBM, SGR recrystallization, and grain rotation.

5. Summary

1. Microstructural analyses were conducted on coarse-grained ice ($\sim 1300\ \mu\text{m}$) deformed under relatively high uniaxial stresses ($>5\ \text{MPa}$). Within deformed samples, kink domains (high-aspect-ratio grains) are widely developed. Recrystallized (small, low-aspect-ratio) grains also form primarily via subgrain rotation recrystallization, further contributing to grain size reduction. Thus, SGR and kinking both contribute to grain segmentation and grain size reduction.

2. Kink bands are composed of both low- ($<10^\circ$) and high-angle (mostly $10\text{--}20^\circ$, many $>20^\circ$) components. Kink band boundaries have misorientation axes lying predominately within the ice basal plane. We suggest that kinking and subgrain rotation follow similar kinematics. Together, these observations suggest that kinking and subgrain rotation can evolve to moderately large misorientation angles while maintaining a near-constant misorientation axis. Other processes (e.g., grain boundary sliding, grain boundary migration) may therefore need to be invoked to explain the randomization of misorientation axes within recrystallized grain networks.

3. Kink domains are preferentially oriented with c -axes sub-perpendicular to the compression axis, unlike remnant grains that have weak cluster and narrow cone-shaped c -axis distributions centred around the compression axis, and nucleated grains that have near-random c -axis distributions. Bulk crystallographic fabrics most closely resemble the CPO of remnant grains, suggesting that kinking does not significantly modify bulk CPOs, at least at the low strains investigated here.

4. Kink band densities decrease monotonically as a function of the angle between the host grain basal plane and the compression axis. Kink domains are nearly absent in grains with basal planes sub-perpendicular to the compression axis, consistent with kink models showing that grains with easy-slip planes (i.e., basal planes, in this case) sub-perpendicular to shortening are fundamentally stable and uneasy to kink since the critical shear stress required for kinking exceeds the applied stress. Grains with basal planes sub-parallel to shortening, on the other hand, have the highest kink band densities. This observation is not expected from models that solely consider strain accommodation via kinking—instead, models suggest that grains with basal planes sub-parallel to shortening

should be harder to kink than grains with basal planes oblique to shortening. We propose that the inconsistency between kink model predictions and experimental observations may be reconciled by considering the activity of both kinking and dynamic recrystallization during deformation. For grains with basal planes oblique to compression (i.e., in easy-slip orientations), strain-induced grain boundary migration (GBM) might be sufficient to relax intragranular strain incompatibilities, reducing the driving force for kinking. For grains with basal planes sub-parallel to compression (i.e., in hard-slip orientations), on the other hand, strain-induced GBM should be inhibited; consequently, strain incompatibilities can be relaxed via kinking.

CRedit authorship contribution statement

Sheng Fan: Conceptualization, Data curation, Formal analysis, Funding acquisition, Methodology, Software, Writing – original draft, Writing – review & editing. **David J. Prior:** Conceptualization, Funding acquisition, Methodology, Supervision, Writing – review & editing. **Travis F. Hager:** Data curation, Methodology. **Andrew J. Cross:** Methodology, Software, Writing – review & editing. **David L. Goldsby:** Funding acquisition, Methodology, Supervision. **Marianne Negrini:** Data curation, Writing – review & editing.

Declaration of competing interest

The authors declare that they have no known competing financial interests or personal relationships that could have appeared to influence the work reported in this paper.

Data availability

Data can be obtained via Mendeley Data (<https://doi.org/10.17632/tstn4krkt8.1>; Fan et al., 2021).

Acknowledgements

We are thankful to Pat Langhorne for providing the cold-room facility at University of Otago. This work was supported by a NASA fund (grant no. NNX15AM69G) to David L. Goldsby and two Marsden Funds of the Royal Society of New Zealand (grant nos. UOO1116, UOO052) to David J. Prior. Sheng Fan was supported by the University of Otago doctoral scholarship, the Antarctica New Zealand doctoral scholarship, a research grant from New Zealand Ministry of Business, Innovation and Employment through the Antarctic Science Platform (ANTA1801) (grant no. ASP-023-03), and a New Zealand Antarctic Research Institute (NZARI) Early Career Researcher Seed Grant (grant no. NZARI 2020-1-5). We thank Marco Herwegh and an anonymous reviewer and editor Alex Webb for their insightful reviews and editorial handling that helped to improve the manuscript.

Appendix A. Technical details of ice sample preparation and cryo-EBSD data collection

Samples were first cut in a -20°C cold room using a band saw. During this step, samples were stored in $\sim 100^{\circ}\text{C}$ liquid nitrogen mist when not being cut. Ice samples were cut in half along the cylinder axis, and a 5 mm thick slice was extracted from half of the sample. One of these halves was returned to the liquid nitrogen dewar for archive storage. The cutting time for each sample was <5 minutes. One side of each ice slice, at a temperature of -30 to -50°C , was placed against a copper ingot at $\sim 5^{\circ}\text{C}$, forming a bond. Ice-ingot assemblies were immediately returned to the liquid nitrogen mist once fully bonded. Polished sample surfaces were subsequently acquired by hand lapping at $\sim 40^{\circ}\text{C}$ on sandpapers

with grit sizes of 80, 240, 600, 1200 and 2400. After polishing, ice-ingot assemblies were stored at liquid nitrogen temperature before being transferred to a scanning electron microscope (SEM) for cryo-EBSD data acquisition.

We collected EBSD data from the polished surface of each ice sample in the University of Otago. A Zeiss Sigma VP FEG-SEM combined with an Oxford Instruments' Symmetry EBSD camera was used for the data collection. The ice-ingot assembly was transferred to a cold SEM stage maintained at $\sim -100^{\circ}\text{C}$. Pressure cycling in the SEM chamber was performed to remove frost and create a damage-free sample surface via sublimation (Prior et al., 2015). Raw EBSD data were collected with a step size of $5\ \mu\text{m}$ at a stage temperature of $\sim -95^{\circ}\text{C}$, with 2–5 Pa nitrogen gas pressure, 30 kV accelerating voltage and ~ 60 nA beam current. EBSD maps were indexed (as ice-1h) at a typical rate of $\sim 90\%$. Raw EBSD data were montaged using the Oxford Instruments' AZtec software.

Appendix B. Supplementary material

Supplementary material related to this article can be found online at <https://doi.org/10.1016/j.epsl.2021.117136>.

References

- Bachmann, F., Hielscher, R., Schaeben, H., 2011. Grain detection from 2d and 3d EBSD data—specification of the MTEX algorithm. *Ultramicroscopy* 111, 1720–1733. <https://doi.org/10.1016/j.ultramic.2011.08.002>.
- Barsoum, M.W., 2020. Ripplifications: a progress report. *Front. Mater.* 7, 1–17. <https://doi.org/10.3389/fmats.2020.00146>.
- Bell, I.A., Wilson, C.J.L., McLaren, A.C., Etheridge, M.A., 1986. Kinks in mica: role of dislocations and (001) cleavage. *Tectonophysics* 127, 49–65. [https://doi.org/10.1016/0040-1951\(86\)90078-8](https://doi.org/10.1016/0040-1951(86)90078-8).
- Bestmann, M., Prior, D.J., 2003. Intragranular dynamic recrystallization in naturally deformed calcite marble: diffusion accommodated grain boundary sliding as a result of subgrain rotation recrystallization. *J. Struct. Geol.* 25, 1597–1613. [https://doi.org/10.1016/S0191-8141\(03\)00006-3](https://doi.org/10.1016/S0191-8141(03)00006-3).
- Burkhard, M., 1993. Calcite twins, their geometry, appearance and significance as stress-strain markers and indicators of tectonic regime: a review. *J. Struct. Geol.* 15, 351–368. [https://doi.org/10.1016/0191-8141\(93\)90132-T](https://doi.org/10.1016/0191-8141(93)90132-T).
- Chauve, T., Montagnat, M., Barou, F., Hidas, K., Tommasi, A., Mainprice, D., 2017a. Investigation of nucleation processes during dynamic recrystallization of ice using cryo-EBSD. *Philos. Trans. R. Soc., Math. Phys. Eng. Sci.* 375. <https://doi.org/10.1098/rsta.2015.0345>.
- Chauve, T., Montagnat, M., Piazzolo, S., Journaux, B., Wheeler, J., Barou, F., Mainprice, D., Tommasi, A., 2017b. Non-basal dislocations should be accounted for in simulating ice mass flow. *Earth Planet. Sci. Lett.* 473, 247–255.
- Cole, D.M., 1979. Preparation of polycrystalline ice specimens for laboratory experiments. *Cold Reg. Sci. Technol.* 1, 153–159. [https://doi.org/10.1016/0165-232X\(79\)90007-7](https://doi.org/10.1016/0165-232X(79)90007-7).
- Derby, B., Ashby, M.F.F., 1987. On dynamic recrystallisation. *Scr. Metall.* 21, 879–884. [https://doi.org/10.1016/0036-9748\(87\)90341-3](https://doi.org/10.1016/0036-9748(87)90341-3).
- Drury, M.R., Pennock, G.M., 2007. Subgrain rotation recrystallization in minerals. *Mater. Sci. Forum* 550, 95–104. <https://doi.org/10.4028/www.scientific.net/msf.550.95>.
- Duval, P., Ashby, M.F., Anderman, I., 1983. Rate-controlling processes in the creep of polycrystalline ice. *J. Phys. Chem.* 87, 4066–4074. <https://doi.org/10.1021/j100244a014>.
- Falus, G., Tommasi, A., Soustelle, V., 2011. The effect of dynamic recrystallization on olivine crystal preferred orientations in mantle xenoliths deformed under varied stress conditions. *J. Struct. Geol.* 33, 1528–1540.
- Fan, S., Hager, T.F., Prior, D.J., Cross, A.J., Goldsby, D.L., Qi, C., Negrini, M., Wheeler, J., 2020. Temperature and strain controls on ice deformation mechanisms: insights from the microstructures of samples deformed to progressively higher strains at -10 , -20 and -30°C . *Cryosphere* 14, 3875–3905. <https://doi.org/10.5194/tc-14-3875-2020>.
- Fan, S., Prior, D.J., Cross, A.J., Goldsby, D.L., Hager, T.F., Negrini, M., Qi, C., 2021. Using grain boundary irregularity to quantify dynamic recrystallization in ice. *Acta Mater.* 209, 116810. <https://doi.org/10.1016/j.actamat.2021.116810>.
- Ferrill, D.A., Morris, A.P., Evans, M.A., Burkhard, M., Groshong, R.H., Onasch, C.M., 2004. Calcite twin morphology: a low-temperature deformation geothermometer. *J. Struct. Geol.* 26, 1521–1529. <https://doi.org/10.1016/j.jsg.2003.11.028>.
- Gay, N.C., Weiss, L.E., 1974. The relationship between principal stress directions and the geometry of kinks in foliated rocks. *Tectonophysics* 21, 287–300. [https://doi.org/10.1016/0040-1951\(74\)90056-0](https://doi.org/10.1016/0040-1951(74)90056-0).

- Halfpenny, A., Prior, D.J., Wheeler, J., 2006. Analysis of dynamic recrystallization and nucleation in a quartzite mylonite. *Tectonophysics* 427, 3–14. <https://doi.org/10.1016/j.tecto.2006.05.016>.
- Heard, H.C., Durham, W.B., Boro, C.O., Kirby, S.H., 1990. A triaxial deformation apparatus for service at $77 \leq T \leq 273$ K. In: *The Brittle-Ductile Transition in Rocks*, pp. 225–228.
- Herwegh, M., de Bresser, J.H.P., ter Heege, J.H., 2005. Combining natural microstructures with composite flow laws: an improved approach for the extrapolation of lab data to nature. *J. Struct. Geol.* 27, 503–521. <https://doi.org/10.1016/j.jsg.2004.10.010>.
- Herwegh, M., Handy, M.R., Heilbronner, R., 1997. Temperature- and strain-rate-dependent microfabric evolution in monomineralic mylonite: evidence from in situ deformation of norcamphor. *Tectonophysics* 280, 83–106. [https://doi.org/10.1016/S0040-1951\(97\)00139-X](https://doi.org/10.1016/S0040-1951(97)00139-X).
- Hidas, K., Tommasi, A., Mainprice, D., Chauve, T., Barou, F., Montagnat, M., 2017. Microstructural evolution during thermal annealing of ice-I h. *J. Struct. Geol.* 99, 31–44. <https://doi.org/10.1016/j.jsg.2017.05.001>.
- Honea, E., Johnson, A.M., 1976. A theory of concentric, kink and sinusoidal folding and of monoclinical flexuring of compressible, elastic multilayers: IV. Development of sinusoidal and kink folds in multilayers confined by rigid boundaries. *Tectonophysics* 30, 197–239. [https://doi.org/10.1016/0040-1951\(76\)90187-6](https://doi.org/10.1016/0040-1951(76)90187-6).
- Humphreys, F.J., Hatherly, M., Rollett, A., 2017. *Recrystallization and Related Annealing Phenomena*, third. ed. Elsevier Ltd.
- Jansen, D., Llorens, M.G., Westhoff, J., Steinbach, F., Kipfstuhl, S., Bons, P.D., Griera, A., Weikusat, I., 2016. Small-scale disturbances in the stratigraphy of the NEM ice core: observations and numerical model simulations. *Cryosphere* 10, 359–370. <https://doi.org/10.5194/tc-10-359-2016>.
- Journaux, B., Kalousová, K., Sotin, C., Tobie, G., Vance, S., Saur, J., Bollengier, O., Noack, L., Rückriemen-Bez, T., Van Hoolst, T., Soderlund, K.M., Brown, J.M., 2020. Large ocean worlds with high-pressure ices. *Space Sci. Rev.* 216. <https://doi.org/10.1007/s11214-019-0633-7>.
- Kamb, B., 1972. Experimental recrystallization of ice under stress. In: *Flow and Fracture of Rocks*. American Geophysical Union, pp. 211–241.
- Lacombe, O., 2010. Les macles de la calcite, un outil pour les études tectoniques dans les chaînes plissées et les avant-pays peu déformés des orogènes. *Oil Gas Sci. Technol.* 65, 809–838. <https://doi.org/10.2516/ogst/2009088>.
- Marano, A., Gélébart, L., Forest, S., 2021. FFT-based simulations of slip and kink bands formation in 3D polycrystals: influence of strain gradient crystal plasticity. *J. Mech. Phys. Solids* 149, 104295. <https://doi.org/10.1016/j.jmps.2021.104295>.
- Monz, M.E., Hudleston, P.J., Prior, D.J., Michels, Z., Fan, S., Negrini, M., Langhorne, P.J., Qi, C., 2021. Full crystallographic orientation (c and a axes) of warm, coarse-grained ice in a shear-dominated setting: a case study. *Cryosphere* 15, 303–324. <https://doi.org/10.5194/tc-15-303-2021>.
- Nishikawa, O., Takeshita, T., 1999. Dynamic analysis and two types of kink bands in quartz veins deformed under subgreenschist conditions. *Tectonophysics* 301, 21–34. [https://doi.org/10.1016/S0040-1951\(98\)00219-4](https://doi.org/10.1016/S0040-1951(98)00219-4).
- Piazolo, S., Montagnat, M., Grennerat, F., Moulinc, H., Wheeler, J., 2015. Effect of local stress heterogeneities on dislocation fields: examples from transient creep in polycrystalline ice. *Acta Mater.* 90, 303–309. <https://doi.org/10.1016/j.actamat.2015.02.046>.
- Poirier, J.-P., Guillopé, M., 1979. Deformation induced recrystallization of minerals. *Bull. Minéral.* 102, 67–74. <https://doi.org/10.3406/bulmi.1979.7256>.
- Poirier, J.P., Nicolas, A., 1975. Deformation-induced recrystallization due to progressive misorientation of subgrains, with special reference to mantle peridotites. *J. Geol.* 83, 707–720. <https://doi.org/10.1086/628163>.
- Prior, D.J., 1999. Problems in determining the misorientation axes, for small angular misorientations, using electron backscatter diffraction in the SEM. *J. Microsc.* 195, 217–225. <https://doi.org/10.1046/j.1365-2818.1999.00572.x>.
- Prior, D.J., Lilly, K., Seidemann, M., Vaughan, M., Becroft, L., Easingwood, R., Diebold, S., Obbard, R., Daghlian, C., Baker, I., Caswell, T., Golding, N., Goldsby, D., Durham, W.B., Piazzolo, S., Wilson, C.J.L., 2015. Making EBSD on water ice routine. *J. Microsc.* 259, 237–256. <https://doi.org/10.1111/jmi.12258>.
- Qi, C., Goldsby, D.L., Prior, D.J., 2017. The down-stress transition from cluster to cone fabrics in experimentally deformed ice. *Earth Planet. Sci. Lett.* 471, 136–147. <https://doi.org/10.1016/j.epsl.2017.05.008>.
- Ree, J.H., 1994. Grain boundary sliding and development of grain boundary openings in experimentally deformed octachloropropane. *J. Struct. Geol.* 16, 403–418. [https://doi.org/10.1016/0191-8141\(94\)90044-2](https://doi.org/10.1016/0191-8141(94)90044-2).
- Schmid, S.M., 1994. Textures of geological materials: computer model predictions versus empirical interpretations based on rock deformation experiments and field studies. In: Bunge, H.J., Siegesmund, S., Skrotzki, W., Weber, K. (Eds.), *Textures of Geological Materials*. Informationsgesellschaft Verlag, pp. 279–301.
- Seidemann, M., Prior, D.J., Golding, N., Durham, W.B., Lilly, K., Vaughan, M.J., 2020. The role of kink boundaries in the deformation and recrystallisation of polycrystalline ice. *J. Struct. Geol.* 136, 104010. <https://doi.org/10.1016/j.jsg.2020.104010>.
- Skemer, P., Katayama, I., Jiang, Z., Karato, S.I., 2005. The misorientation index: development of a new method for calculating the strength of lattice-preferred orientation. *Tectonophysics* 411, 157–167. <https://doi.org/10.1016/j.tecto.2005.08.023>.
- Urai, J.L., Means, W.D., Lister, G.S., 1986. Dynamic recrystallization of minerals. In: *Mineral and Rock Deformation: Laboratory Studies*, pp. 161–199.
- Vernon, R.H., 2018. *A Practical Guide to Rock Microstructure*, 2nd ed. Cambridge University Press.
- Warren, J.M., Hirth, G., 2006. Grain size sensitive deformation mechanisms in naturally deformed peridotites. *Earth Planet. Sci. Lett.* 248, 438–450. <https://doi.org/10.1016/j.epsl.2006.06.006>.
- Weertman, J., 1983. Creep deformation of ice. *Annu. Rev. Earth Planet. Sci.* 11, 215–240. <https://doi.org/10.1146/annurev.ea.11.050183.001243>.
- Weiss, J., 2003. Three-dimensional mapping of dislocation avalanches: clustering and space/time coupling. *Science* 80 (299), 89–92. <https://doi.org/10.1126/science.1079312>.
- Wenk, H.-R., Bennett, K., Canova, G.R., Molinari, A., 1991. Modelling plastic deformation of peridotite with the self-consistent theory. *J. Geophys. Res.* 96, 8337. <https://doi.org/10.1029/91JB00117>.
- White, S., 1976. The effects of strain on the microstructures, fabrics, and deformation mechanisms in quartzites. *Philos. Trans. R. Soc. Lond. Ser. A, Math. Phys. Sci.* 283, 69–86.
- Wilson, C.J.L., Peternell, M., Piazzolo, S., Luzin, V., 2014. Microstructure and fabric development in ice: lessons learned from in situ experiments and implications for understanding rock evolution. *J. Struct. Geol.* 61, 50–77. <https://doi.org/10.1016/j.jsg.2013.05.006>.